Article:
Catanzaro, A., Genco, A., Louca, C. et al. (13 more authors) (2024) Resonant band hybridization in alloyed transition metal dichalcogenide heterobilayers. Advanced Materials, 36 (19). 2309644. ISSN 0935-9648

https://doi.org/10.1002/adma.202309644

ADVANCED MATERIALS
www.advmat.de

Resonant Band Hybridization in Alloyed Transition Metal Dichalcogenide Heterobilayers

Alessandro Catanzaro, Armando Genco, Charalambos Louca,* David A. Ruiz-Tijerina,* Daniel J. Gillard, Luca Sortino, Aleksey Kozikov, Evgeny M. Alexeev, Riccardo Pisoni, Lee Hague, Kenji Watanabe, Takashi Taniguchi, Klaus Ensslin, Kostya S. Novoselov, Vladimir Fal'ko, and Alexander I. Tartakovskii**

In memory of Alessandro Catanzaro

Bandstructure engineering using alloying is widely utilized for achieving optimized performance in modern semiconductor devices. While alloying has been studied in monolayer transition metal dichalcogenides, its application in van der Waals heterostructures built from atomically thin layers is largely unexplored. Here, heterobilayers made from monolayers of WSe_2 (or $MoSe_2$) and $Mo_xW_{1-x}Se_2$ alloy are fabricated and nontrivial tuning of the resultant bandstructure is observed as a function of concentration x. This evolution is monitored by measuring the energy of photoluminescence (PL) of the interlayer exciton (IX) composed of an electron and hole residing in different monolayers. In $Mo_xW_{1-x}Se_2/WSe_2$, a strong IX energy shift of ≈100 meV is observed for x varied from 1 to 0.6. However, for $x < 0.6$ this shift saturates and the IX PL energy asymptotically approaches that of the indirect bandgap in bilayer WSe_2. This observation is theoretically interpreted as the strong variation of the conduction band K valley for $x > 0.6$, with IX PL arising from the $K - K$ transition, while for $x < 0.6$, the bandstructure hybridization becomes prevalent leading to the dominating momentum-indirect $K - Q$ transition. This bandstructure hybridization is accompanied with strong modification of IX PL dynamics and nonlinear exciton properties. This work provides foundation for bandstructure engineering in van der Waals heterostructures highlighting the importance of hybridization effects and opening a way to devices with accurately tailored electronic properties.

1. Introduction

Van der Waals stacking allows unprecedented possibilities in combining different atomically thin materials within a single device as well as tuning of their properties, by selecting different monolayer materials or by varying their relative twist angle. Thus, van der Waals (vdW) heterostructures made from vertically stacked atomically thin transition metal dichalcogenides (TMDs) present a powerful platform for development of novel devices with widely tuneable properties[1–3] as well as for gaining new insights in the physics of excitons[4–8] and emergent excitonic and quantum phenomena in moiré superlattices.[9–17] Most of the structures studied so far (such as stacked monolayers of $MoSe_2$ and WSe_2) were so-called type-II semiconducting heterostructures,[18] exhibiting the maximum of the valence and the minimum of the conduction bands in the adjacent layers. A prominent feature in type-II TMD heterostructures is the formation of interlayer excitons (IX)

A. Catanzaro, A. Genco, C. Louca, D. J. Gillard, L. Sortino, E. M. Alexeev, A. I. Tartakovskii
Department of Physics and Astronomy
The University of Sheffield
Sheffield S3 7RH, UK
E-mail: armando.genco@polimi.it; charalambos.louca@polimi.it; a.tartakovskii@sheffield.ac.uk

The ORCID identification number(s) for the author(s) of this article can be found under https://doi.org/10.1002/adma.202309644

DOI: 10.1002/adma.202309644

A. Genco, C. Louca
Dipartimento di Fisica
Politecnico di Milano
Piazza Leonardo da Vinci, 32, Milano 20133, Italy

D. A. Ruiz-Tijerina
Departamento de Física Química
Instituto de Física, Universidad Nacional Autónoma de México
Ciudad de México, C.P., 04510 Mexico, México
E-mail: d.ruiz-tijerina@fisica.unam.mx

L. Sortino
Chair in Hybrid Nanosystems, Nanoinstitute Munich, Faculty of Physics
Ludwig-Maximilians-Universität München
80539 Munich, Germany

A. Kozikov, V. Fal'ko
Department of Physics and Astronomy
University of Manchester
Manchester M13 9PL, UK

with a hole and electron confined in different layers. The IX PL, although observed most clearly at cryogenic temperatures, has proven to be a sensitive probe of the novel physics in semiconducting van der Waals heterostructures,[19,20] and will be utilized in our work to monitor the properties of the studied TMD heterobilayers.

As well as the use of heterostructures, another very powerful approach for accurate tailoring of the properties of semiconductor devices is the use of alloyed semiconductors. This approach has been successfully applied in numerous applications, from lasers to few-nm-sized transistors using traditional III-V, II-VI, and group IV semiconductors.[21] This approach allows gradual tuning of bandgaps as well as the whole bandstructure, allowing to control carrier confinement and thus influence their transport and optical properties. Numerous semiconducting alloys of layered materials have been demonstrated in the monolayer form achieved both by direct synthesis and exfoliation from bulk,[22] including $Mo_xW_{1-x}Se_2$ used in this work, where alloying was used to control the valley polarization properties.[23,24] More recently, alloying was successfully employed to tune the energy of interlayer excitons[25] in $WS_{2(1-x)}Se_{2x}/WSe_2$, and a direct–indirect band transition in $Mo_{1-x}W_xS_2/MoSe_2$ heterostructures has been predicted theoretically.[26]

In our work we study $Mo_xW_{1-x}Se_2/WSe_2$ and $Mo_xW_{1-x}Se_2/MoSe_2$ heterostructures built from stacked TMD monolayers in a wide range of composition x (**Figure 1a**). In $Mo_xW_{1-x}Se_2/WSe_2$, we demonstrate tuning of ≈130 meV of the IX photoluminescence (PL) peak energy as a function of x displaying two types of behavior: a fast tuning by ≈100 meV for $x > 0.6$ followed by an asymptotic dependence for $x < 0.6$, where the IX PL energy asymptotically approaches that of the indirect bandgap in bilayer WSe_2. A similar but less pronounced tuning and saturation at the indirect bandgap of bilayer $MoSe_2$ is observed for $Mo_xW_{1-x}Se_2/MoSe_2$. In $Mo_xW_{1-x}Se_2/WSe_2$, concurrent with the transition between the two types of behavior, we also observe strong changes in the IX PL dynamics and intensity: the PL lifetime shortens and intensity strongly decreases for $x < 0.6$. The strong changes are also observed in the power dependence of IX PL, where a typical blue-shift of the IX PL peak[18] is strongly suppressed for $x < 0.6$. Our theoretical analysis shows that the observed changes in the behavior occur due to the bandstructure hybridization, leading to the shift of the conduction band minimum in the heterobilayer from K to Q valley for $x \approx 0.6$. The observed behavior thus signifies the transition from the $K-K$ configuration of the valence to conduction band transition for $x > 0.6$ to the $K-Q$ configuration for $x < 0.6$.

2. Results

A set of 15 samples was studied, including heterobilayers (HBLs) either fully encapsulated in hBN flakes or alternatively placed on a relatively thick (of the order of 50 nm) hBN. The TMD HBLs were fabricated from monolayers mechanically exfoliated from bulk crystals. The alloy bulk crystals were provided by HQ Graphene, where the material composition was accurately measured in each bulk sample using energy dispersive X-ray (EDX) microanalysis. The majority of HBLs were made with the prominent crystal edges aligned within 0.5° accuracy, constituting structures with either near 0° or 60° crystal axis rotation (referred to as R- and H-stacking, respectively). For further experiments we did not differentiate between R- and H-stacked heterobilayers and measured all fabricated samples. However, our results imply that inadvertently the majority of samples that we fabricated and studied were of the H-stacking configuration. To understand why the yield of fabricated structures may have a tendency toward one of the two orientations we go over the fabrication process in more detail in Note S1 (Supporting Information).

It is likely that the close to 60° or 0° alignment in our HBL samples results in realization of the regime of lattice reconstruction.[27–30] However, the method that we adopted for reporting our PL data (summarized in **Figure 2c**) by averaging PL spectra over 20–60 different locations on each measured HBL, masks the influence of lattice reconstruction on exciton properties, for which we instead refer the reader to Ref. [30]. We also note that lattice reconstruction influences the local shifts of the IX energy.[28–30] However, these shifts are smaller than the IX and band-edge energy shifts as a function of concentration x, and thus only provide a detail in the overall trends of bandstructure modifications with alloy concentration, which we report here.

A schematic of a generic $Mo_xW_{1-x}Se_2/WSe_2$ HBL is displayed in Figure 1b, also showing IX formation with a hole localized in WSe_2 and the electron in the alloy. A bright field (BF) microscope image of a $Mo_{0.85}W_{0.15}Se_2/WSe_2$ heterostructure is shown in Figure 1c. The alloy monolayer area is highlighted with red lines, while the edges of the WSe_2 flake are shown in green. Figure 1d shows a PL image of this sample measured at room temperature showing in yellow bright emission from the uncoupled monolayer WSe_2 and in purple dimmer emission from the uncoupled monolayer $Mo_{0.85}W_{0.15}Se_2$. Notably lower PL intensity

A. Kozikov
School of Mathematics, Statistics and Physics
Newcastle University
Newcastle upon Tyne NE1 7RU, UK
E. M. Alexeev
Cambridge Graphene Centre
University of Cambridge
9 J. J. Thomson Avenue, Cambridge CB3 0FA, UK
R. Pisoni, K. Ensslin
Solid State Physics Laboratory, ETH Zurich
Zurich CH-8093, Switzerland
L. Hague
National Graphene Institute, University of Manchester
Manchester M13 9PL, UK
K. Watanabe
Research Center for Electronic and Optical Materials
National Institute for Materials Science
1-1 Namiki, Tsukuba 305-0044, Japan
T. Taniguchi
Research Center for Materials Nanoarchitectonics
National Institute for Materials Science
1-1 Namiki, Tsukuba 305-0044, Japan
K. S. Novoselov
Institute for Functional Intelligent Materials
National University of Singapore
Singapore 117546, Singapore
V. Fal'ko
Henry Royce Institute for Advanced Materials
University of Manchester
Manchester M13 9PL, United Kingdom

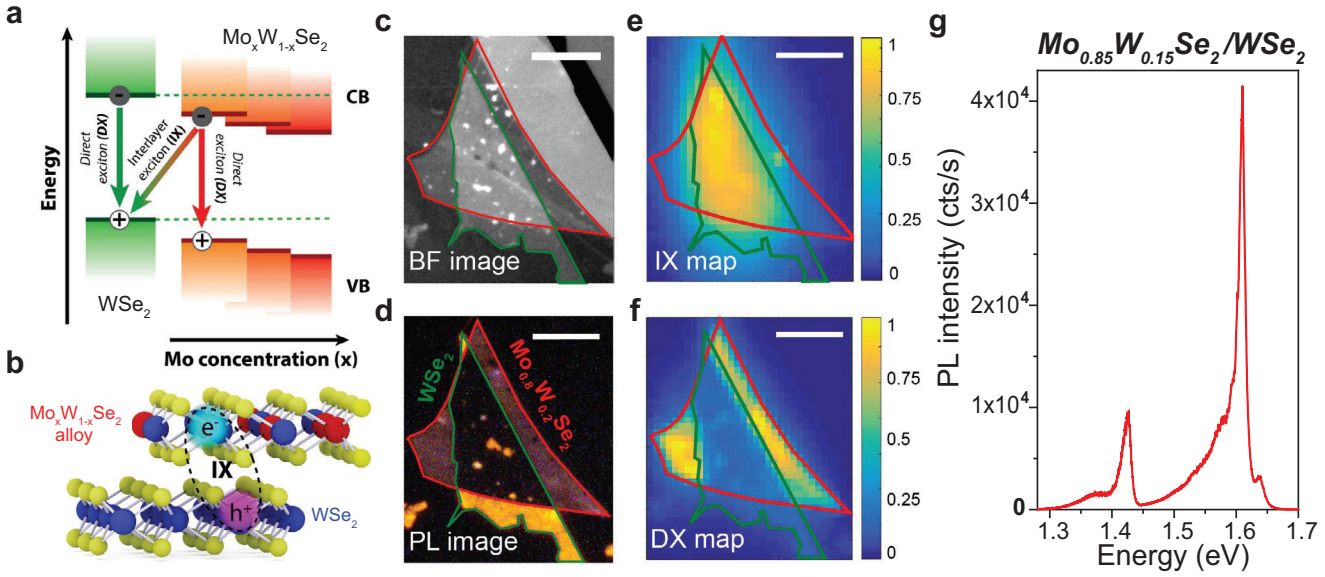

Figure 1. Van der Waals heterostructures based on TMD alloy monolayers. a) Energy level diagram for a type-II heterojunction formed by WSe_2 and $Mo_xW_{1-x}Se_2$ monolayers. Direct excitons (DX) form in each layer, while interlayer excitons (IX) are created between electrons in the conduction band (CB) of the alloy and holes in the valence band (VB) of WSe_2. The IX energy is tuned by changing the Mo composition x in the alloy. b) Schematic of the alloy HBL showing the IX electric dipole moment orientated perpendicular to the plane of the monolayers. c) Bright-field (BF) microscope image of the HBL. The red line shows the $Mo_{0.85}W_{0.15}Se_2$ flake while the green line shows the WSe_2 flake. d) PL image of the HBL taken at room temperature. PL quenching in the HBL region indicates efficient charge transfer between the monolayers. e) Low temperature (T = 10 K) PL map of the HBL in the spectral region of IX PL (1.3–1.45 eV). Bright IX PL is detected from the HBL only. f) Low temperature (10 K) PL map of the HBL in the spectral region of DX PL (1.45–1.7 eV). Scale bars for (c–f) 10 µm. g) Low temperature (10K) spectrum measured for a $Mo_{0.85}W_{0.15}Se_2$ HBL.

is observed in the heterobilayer region where the two monolayers overlap. This arises from the quenching of the PL of the intralayer exciton (referred to below as DX) due to the efficient charge transfer between the layers. This shows efficient electronic coupling between the TMD monolayers, and confirms the formation of a type-II heterostructure.[31–33]

Figure 1e,f shows PL maps of the same HBL acquired at a cryogenic temperature T = 10 K. The maps show integrated PL intensity in the spectral ranges 1.3–1.45 eV in Figure 1e and 1.45–1.7 eV in Figure 1f. These ranges are selected based on the low temperature PL spectra, with a typical example measured in the HBL area shown in Figure 1g. In addition to a strong peak ≈1.6 eV corresponding to the intralayer exciton (DX) in $Mo_{0.85}W_{0.15}Se_2$ and some lower intensity features arising from WSe_2, additional peaks are observed at low energy (labeled IX). These peaks correspond to the interlayer exciton PL and are only observed within the HBL area.

Before describing the properties of HBLs comprising alloy monolayers, we briefly report optical properties of monolayer and bilayer alloy TMDs themselves. Figure 2a shows PL spectra for $Mo_xW_{1-x}Se_2$ alloy monolayers with different composition x. For $0.49 \leqslant x \leqslant 1$, the PL spectra closely resemble that of $MoSe_2$ with two narrow peaks attributed to neutral exciton, X_0 (the spectral feature of A-exciton) and the corresponding charged exciton or trion, X*. For $x \leqslant 0.38$, the PL peaks become much broader, the X* peak becomes much less pronounced, and more features appear at lower energies. This behavior is observed for concentrations for which the lowest neutral exciton state in the alloy transforms from optically bright as in $MoSe_2$ to optically dark as in WSe_2, as previously predicted.[23,34] We have further studied reflectance contrast (RC) spectra from monolayers that allows detection of high energy states, for example, B-excitons (see Note S2, Supporting Information). The A-exciton energy appears almost constant at 1.650 eV for $0.49 \leqslant x \leqslant 1$ with a weak increase toward $x = 1$. For $x < 0.49$, the energy of A peak increases eventually reaching 1.742 eV for monolayer WSe_2. The observed trend can be fitted by the quadratic Vegard's law (Note S2, Supporting Information; Figure 2c), adopted, for example, for alloys of III-V semiconductors,[35] revealing a bowing parameter b = 0.16, in close agreement with previous reports.[36,37] Figure S2 (Supporting Information) shows that the B-exciton energy increases more sharply with decreasing x from 1.877 to 2.185 eV signifying a strong increase in the valence band spin-orbit splitting as the A-B exciton splitting changes from ≈230 to ≈340 meV.

Of high relevance to HBL studies presented in this work we have also measured low T PL and RC for exfoliated $Mo_xW_{1-x}Se_2$ bilayers with different concentration of x (see Note S3, Supporting Information). The RC spectra show a similar behavior of A and B exciton energies compared to monolayers. In Figure 2c, we show a comparison between the A exciton peak positions in monolayers (diamonds) and bilayers (triangles), where similar parabolic trends are observed. However, a systematic red-shift up to 40 meV of the peak positions with respect to the monolayers with the same x occurs.[38] The PL data shows that the momentum-indirect transition is always dominant in bilayers (Note S3, Supporting Information), with its energy tuned by > 100 meV by changing the Mo composition of the bilayer alloy $Mo_xW_{1-x}Se_2$.

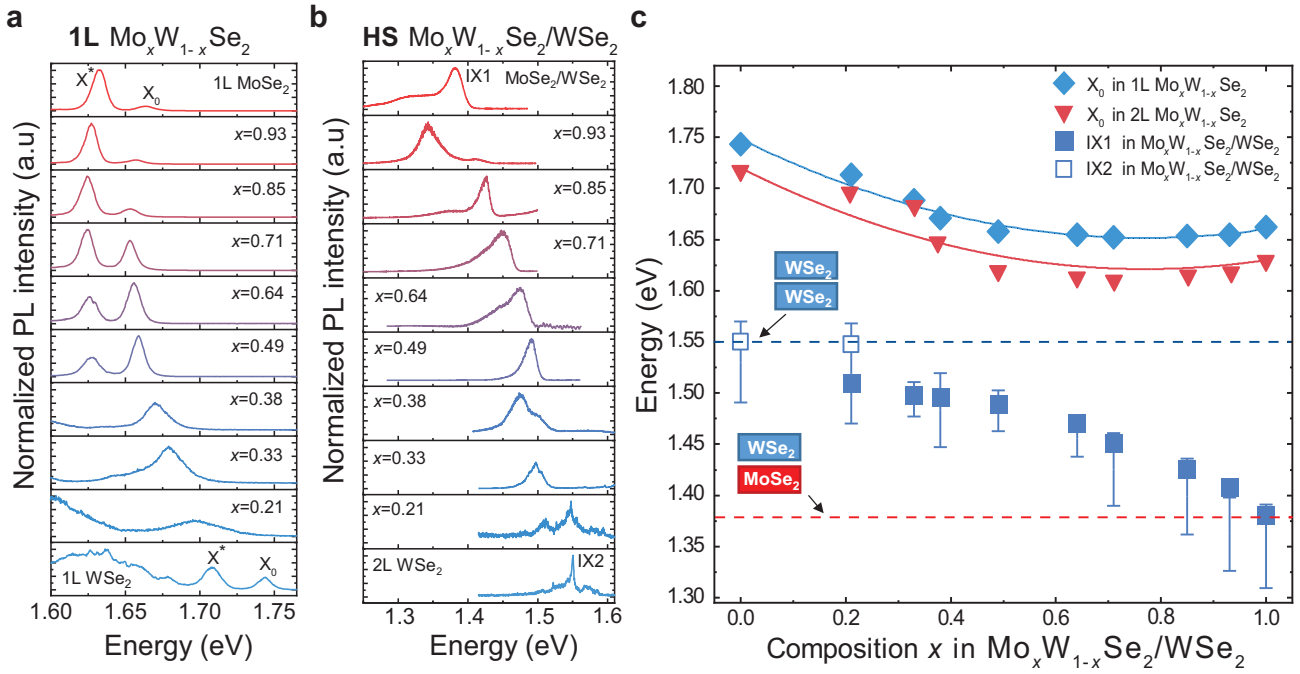

Figure 2. Optical spectra of intralayer and interlayer excitons in alloy monolayers and heterostructures. a) Normalized PL spectra measured at $T = 10$K of $Mo_xW_{1-x}Se_2$ alloy monolayers with different Mo concentrations (x), showing the neutral exciton X_0 and the trion X* peaks. b) Normalized PL spectra of the $Mo_xW_{1-x}Se_2/WSe_2$ HBLs measured at 10K for different x. IX1 and IX2 label the interlayer exciton PL and the PL peak at the indirect bandgap in WSe_2 bilayers, respectively. c) Solid (open) squares show spectral positions of IX1 (IX2) PL peaks in the alloy/WSe_2 HBLs. See text for discussion of the x =0.21 HBL. Error bars show the spread in energy of multiple IX transition peaks measured in several HBL samples (see text for further details). Diamonds (triangles) show X_0 (A-exciton) peak position in alloy monolayers (bilayers) measured using reflectance contrast. Solid light blue and red lines are parabolic fits of the A-exciton peak energy in alloy monolayers and bilayers, respectively. The dashed red and blue horizontal lines correspond to the IX1 PL peak in $MoSe_2/WSe_2$ HBLs and the IX2 PL peak in WSe_2 homobilayers, respectively.

We now discuss the tuning of the interlayer exciton energy in $Mo_xW_{1-x}Se_2/WSe_2$ HBLs as a function of x. Figure 2b shows normalized PL spectra measured for such structures at T = 10 K in the energy range where IX PL is expected, as identified in Figure 1. Similarly to Figure 1g, features corresponding to IX PL can be readily identified in the spectra of all structures with $x \geqslant 0.21$. Following the approach depicted in Figure 1, we measured PL maps at low temperature on all the structures to ensure that these features could be observed only in the regions where the two TMDs overlap (see Note S4, Supporting Information). For all HBLs with $x > 0.33$, IX PL shows a spectrum with two or more peaks, similar to those reported for $MoSe_2/WSe_2$ heterostructures.[11,18,30,39,40] The energies of these PL peaks increase with decreasing x (see further peak analysis of the IX spectra and a detailed discussion of the origin of the different spectral features in Note S5, Supporting Information). The tuning is pronounced for x up to 0.64 and exceeds 100 meV, but then slows down and is less than 50 meV for the whole range of $x < 0.64$.

For $x = 0.33$, these peaks practically merge into a single peak at ≈1.5 eV. For $x = 0.21$, a peak at ≈1.51 eV provides a continuation of this trend, while new structured PL appears at higher energy at and above 1.54 eV. Similar high energy PL peaks are also observed at ≈1.54 and 1.57 eV in the natural (as exfoliated) WSe_2 bilayer[41] (see the spectrum labeled 2L in the figure), while no discernible PL occurs in this sample at lower energies, where IX PL is observed in samples with $x > 0$. Except for the IX feature at ≈1.51 eV in the $x = 0.21$ structure, the spectra for the structures with $x = 0.21$ and $x = 0$ are similar to the one reported for another WSe_2 bilayer in Figure S3 (Supporting Information), measured on a different sample.

Spectra similar to the ones reported in Figure 2b were measured on 20 to 60 points across each HBL. Notably, the PL intensity averaged across the measured points of each HBL drops significantly for $x < 0.6$ (see Note S6, Supporting Information). For some values of x, we also made several samples where similar PL measurements were carried out at multiple positions providing similar results.

We note that PL data reported in Figure 2b show qualitatively different spectra for different samples. Whereas the $x = 0.93$ and $x = 0.38$ samples show a two-peak structure with the low-energy peak exhibiting higher PL intensity, other samples exhibit two-peak PL spectra with a more pronounced high-energy peak (see further details of the fitting in Figure S8, Supporting Information). This may indicate that the $x = 0.93$ and $x = 0.38$ samples have a different stacking configuration from the rest.[30,42] To further explore this possibility, in Note S5 (Supporting Information), we present an explanation of the two-peak structure found in our interlayer exciton PL measurements of Figure 2b supporting our overall conclusion that most of the structures studied in this work had a 60° mutual rotation of the alloy and WSe_2 monolayers, i.e., displayed the H-stacking, which we believe was a result of specifics of the fabrication procedure described in Note S1 (Supporting Information).

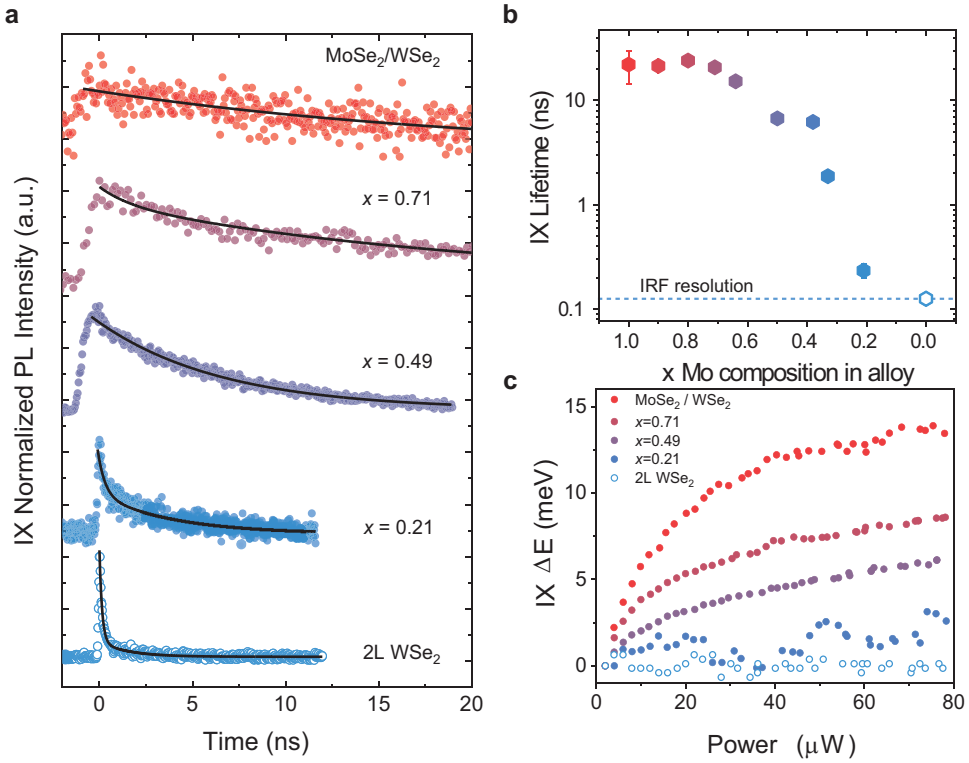

Figure 3. Time-resolved and power-dependent PL of interlayer excitons in $Mo_xW_{1-x}Se_2/WSe_2$ heterostructures. a) Time-resolved PL traces of IX in $Mo_xW_{1-x}Se_2/WSe_2$ HBLs with different x measured at $T = 10$ K. Fitting with a single ($x = 1$, 0.49) or double ($x = 0.71$, 0.21, 0) exponential decay are shown with black lines. b) IX PL decay times as a function of x for $Mo_xW_{1-x}Se_2/WSe_2$ HBLs extracted from the data in (a). The dashed line indicates the temporal resolution limit given by the instrument response function (IRF) of the experimental setup. c) Energy shift of the IX peak in $Mo_xW_{1-x}Se_2/WSe_2$ HBLs with different x as a function of the excitation power.

The PL peak positions averaged over many measurements at different locations within each HBL are presented in Figure 2c. Here the squares show the average high energy peak position of the IX1 PL (E_{IX}), ascribed in $MoSe_2/WSe_2$ HBLs to the momentum-direct K-K transition.[11,39,40] The vertical bars show the spectral extension of the PL intensity within a standard deviation from the average intensity, covering all the features observed in the spectra near the IX energy. Overall, we observe that E_{IX} changes with decreasing x by 130 meV from 1.38 eV for $MoSe_2/WSe_2$ to 1.51 eV for $Mo_{0.21}W_{0.79}Se_2/WSe_2$. This is in contrast to a weak dependence of the $Mo_xW_{1-x}Se_2$ bandgap (as can be deduced from a weak dependence of the X_0 exciton energy presented in the same plot) for $0.5 < x \leqslant 1$. Thus, in this range of x the conduction band offset of $Mo_xW_{1-x}Se_2$ with respect to that of WSe_2 evidently experiences a much faster change, with a shift by more than 100 meV, as can be deduced from the increase of E_{IX} (assuming weak dependencies of the IX and DX exciton binding energies on x).[43] It is seen from Figure 2c that the dependence of E_{IX} on x is nonlinear and asymptotically approaches 1.51 eV, close to the energy of the exciton transition at the indirect bandgap in the homobilayer of WSe_2 marked IX2 in Figure 2b and shown with open squares in Figure 2c.

We also fabricated several $Mo_xW_{1-x}Se_2/MoSe_2$ HBLs, where a more complicated behavior is observed for $0.33 < x \leqslant 1$, with less distinct PL peaks in the range where IX PL is expected (see Note S7, Supporting Information). However, with increasing x, the main feature of the low energy PL response asymptotically approaches the energy corresponding to PL at the indirect bandgap in homobilayer $MoSe_2$, similarly to the $Mo_xW_{1-x}Se_2/WSe_2$ HBLs.

In order to understand the nature of the low energy PL peaks in the studied HBLs and to gain further insight in the properties of the IX as a function of the alloy composition, we carried out time-resolved and power-dependent PL measurements. The transient PL decay signals measured for $Mo_xW_{1-x}Se_2/WSe_2$ HBLs are shown in **Figure** 3a. Each transient PL decay curve is measured at the IX1 PL peak shown in Figure 2c. For $Mo_{0.21}W_{0.79}Se_2/WSe_2$ structure, we measure at the energy of 1.51 eV corresponding to the energy of IX1 (solid square in Figure 2c). For the WSe_2 bilayer the measurement is carried out at the PL peak around 1.55 eV (IX2, open squares in Figure 2c).

It can be observed that the PL decay of the IX shortens progressively, decreasing from tens of nanoseconds in $MoSe_2/WSe_2$ down to hundreds of picoseconds in the $Mo_{0.21}W_{0.79}Se_2/WSe_2$ HBL and bilayer WSe_2. The lifetime values extracted from exponential fits of the time-resolved PL curves are summarized in Figure 3b as a function of the alloy composition (see further details on the results of the fitting in Note S8, Supporting Information). As the alloys gradually become more chemically similar to WSe_2, the PL lifetime decreases by more than two orders of magnitude, with the most abrupt change occurring for $x < 0.4$. The fast decay times extracted for the WSe_2 bilayer are limited by the

temporal resolution of the set-up (shown with a dashed line in Figure 3b) and are in agreement with the 25 ps lifetime previously reported for WSe_2 bilayers.[44] Such a strong reduction of the PL lifetime may arise from two related effects. First, a similar effect has been observed in a gated bilayer WSe_2,[45] where the application of a vertical electric field induces an increase of the interlayer exciton lifetime, directly related to the enhanced spatial confinement of the carriers in the adjacent layers. In our case, gradual tuning of the bandstructure towards that of a WSe_2 bilayer should result in an increased spatial overlap of the electron and hole wavefunctions, leading to interlayer excitons with shorter lifetimes. On the other hand, as we discuss below, a gradual transition to the indirect bandgap semiconductor with decreasing x should lead to strong nonradiative decay,[46] as additionally evidenced by the reduction of the overall PL emission in HBLs with small x (see Figure S11, Supporting Information).

Further confirmation of this interpretation is obtained from the power dependence of the spectral position of the IX PL, which can be used to assess the efficiency of the exciton–exciton interaction between IXs. The IXs possess permanent dipole moments, aligned along the direction normal to the plane of the device, resulting in enhanced repulsive dipolar exciton-exciton interactions.[18] This gives rise to a blue-shift of the IX PL peak energy at sufficiently high excitation density, i.e., for high IX densities. Above a certain power, both the blue-shift and the PL intensity saturate, due to the exciton-exciton annihilation processes.[47] Figure 3c shows experimentally measured blue-shift as a function of the power of a continuous-wave laser in several HBLs with different x. We observe a maximum shift of 14 meV in a $MoSe_2/WSe_2$ structures at the excitation power of 80 μW in agreement with previously reported values.[18] The shift progressively decreases for smaller x and as the heterobilayer becomes more similar to a homobilayer, the blue-shift gradually disappears. At the same time, the power-dependences of PL intensities, showing saturation for high Mo concentrations, become nearly linear as x decreases (see Note S9, Supporting Information).

We believe that these observations support the conclusions derived from the PL dynamics. For decreasing x, the electron and hole within the IX-like particle become less localized in the individual layers. This will lead to a smaller dipole moment and thus weaker exciton-exciton interaction and a reduced blue-shift. At the same time, and possibly with a stronger influence on the observed behavior, as the bandgap becomes indirect at small Mo concentrations, the fast non-radiative decay (e.g., caused by carrier relaxation into the Q valley) prevents build-up of the exciton population thus suppressing the exciton–exciton interactions and the corresponding blue-shift.

3. Discussion

We now further analyze the PL data and interpret the asymptotic behavior of the IX energy as a function of x. The conduction- and valence band energy offsets between the WSe_2 and alloy layers forming a given HBL, $\Delta E1$ and $\Delta E2$, can be computed by subtracting the HBL bandgap from the intralayer bandgaps of the WSe_2 and alloy layers, respectively (see the diagram in **Figure** 4a). To this end, we estimate the HBL bandgap as the IX energy, and the intralayer gaps by the corresponding direct exciton energies, as obtained from PL measurements reported in Figure 2a,b. In this approximation, we are neglecting the exciton binding energies and their x dependences,[43] thus incurring an error of the order of tens of meV. The experimental x-dependent energy offsets $\Delta E1$ and $\Delta E2$ are reported in Figure 4a, where two distinct trends can be observed for both curves, one for $0 \leqslant x \lesssim 0.6$ and another for $0.6 \lesssim x \leqslant 1$.

The band offset trends measured for $0.6 \lesssim x \leqslant 1$ can be explained by simple interpolation of the conduction and valence band edge energies of the alloy, assigning a linear trend to the latter, and a quadratic trend to the former with the same bowing parameter measured for the direct A exciton in the alloy.[35] Such interpolation neglects the effects of hybridization between the WSe_2 and alloy layers, and assumes that, as is the case in $MoSe_2/WSe_2$ ($x = 1$),[13,40] the HBL bandgap remains at the K point for all values of x. Full details of this approximation can be found in Note S10 (Supporting Information). The resulting interpolations, shown with solid and dashed lines in Figure 4a, match the experimental trends for $\Delta E1$ and $\Delta E2$ only for $0.6 \lesssim x \leqslant 1$, indicating that interlayer hybridization in the HBL is weak for this range of Mo compositions, and that, indeed, the HBL bandgap remains at the K point. However, continuing the interpolation down to $x \lesssim 0.6$ we find a clear and dramatic deviation from the experimental values, where the predicted offsets (dashed lines in Figure 4a) vanish for $x = 0$, while the experimental values (circles in Figure 4a) converge at a saturation value around 200 meV. This deviation can be explained only if we consider major modifications to the HBL bandstructure for $0 \leqslant x \lesssim 0.6$, such as a transition to an indirect bandgap for the HBL, caused by strong interlayer hybridization at the Γ and Q points of the Brillouin zone.[48]

To explore this possibility, we have formulated simple Hamiltonians for interlayer hybridization of the WSe_2 and alloy bands in the HBL, at the K (conduction and valence), Γ (valence) and Q (conduction) points, with parameters based on density functional theory calculations extracted from Ref. [29]. It is worthwhile mentioning that these models contain no free parameters. Further model details can be found in Note 10 (Supporting Information). Importantly, symmetry considerations[29] dictate that the model parameters differ for HBLs with interlayer angles close to 0° and 60°. We have determined that the best match to the experimental data is obtained assuming HBLs with 60° alignment (see Figure S18 and Note S10, Supporting Information), and limit our discussion to that case. The corresponding predictions for the band offsets $\Delta E1$ and $\Delta E2$, shown with red and black diamonds in Figure 4a, give an excellent quantitative match to the experimental data throughout the full range of compositions, and importantly with the saturation value of ≈200 meV at $x = 0$. The model shows that the HBL conduction band edge migrates from the K to the Q point for $x < 0.65$, whereas the HBL valence band edge remains at the K point, as illustrated in Figure 4b, consistent with recent theoretical reports for WSe_2 bilayers.[29] This results in an indirect ($K - Q$) bandgap that changes the nature of the IX, thus shedding light on the change of trend of $\Delta E1$ and $\Delta E2$, the band offset saturation for $x = 0$, and the suppression of the IX energy tuning with x for Mo concentrations below 0.65. Moreover, the quantitative agreement between the model and experimental data strongly suggests that the samples studied are approximately H-stacked HBLs, with an interlayer twist angle close to 60°.

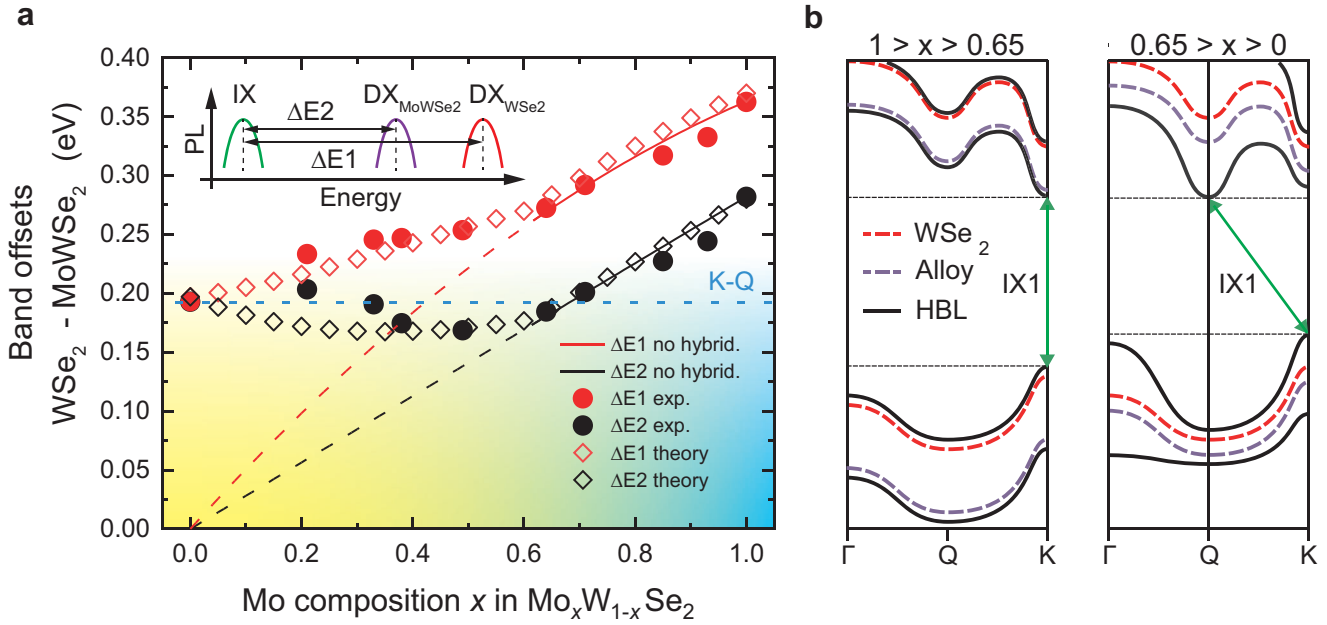

Figure 4. Band offsets of the $Mo_xW_{1-x}Se_2/WSe_2$ HBLs. a) Band offsets of $Mo_xW_{1-x}Se_2/WSe_2$ HBLs as functions of Mo composition x in the alloy layers. The band offsets ΔE1 and ΔE2 are extracted as shown in the diagram in **a** from the experimentally measured PL peaks of IX in the HBLs and direct excitons DX_{MoWSe_2} in alloys and DX_{WSe_2} in WSe_2 measured in isolated monolayers. Experimentally measured ΔE1 and ΔE2 are displayed as filled red and black circles, respectively. Red (black) solid and dashed lines show theoretical values for the conduction (valence) band offsets, obtained assuming a direct HBL bandgap at the *K* point, and neglecting interlayer band hybridization. The experimental energy offsets deviate significantly from the predicted trend for $x \lesssim 0.6$, suggesting strong interlayer band hybridization for that range of Mo concentrations. Empty diamonds show the theoretically predicted trends for Δ*E*1 and Δ*E*2 when interlayer hybridization at the *K*, *Q* and Γ points of the Brillouin zone is considered, assuming an interlayer angle of 60°, showing excellent agreement with the experimental data for all *x* values. b) Sketch of the *x*-dependent HBL bandstructure evolution, according to the interlayer band hybridization model. Dashed (solid) lines indicate the monolayer (HBL) band energies. Whereas for $x > 0.65$ the HBL remains direct due to weak hybridization at the *K* point, strong hybridization of conduction states shifts the conduction band edge to the *Q* point for $x < 0.65$, resulting in an indirect $K - Q$ bandgap, and a finite momentum for the IX.

We now briefly comment on the simultaneous observation of IX1 peak and a high energy PL feature ≈1.55 eV (similar to IX2 in bilayer WSe_2) in the HBL with $x = 0.21$. While IX1 PL originates from the $K - Q$ transition, as suggested above, the following options for the origin of the 1.55 eV feature may be proposed. As can be deduced from the broad spectral features in $Mo_{0.21}W_{0.79}Se_2/WSe_2$ alloy mono- and bilayers, this material is highly disordered. This may lead to occurrence of W-rich clusters, which will locally behave as WSe_2 bilayers, thus giving rise to PL at the IX2 energy. Another explanation, assuming a more even distribution of Mo in the alloy is related to PL emission involving $\Gamma - Q$ transition, expected around 50 meV higher than $K - Q$, and activated in this alloy either due to the increased disorder or a relatively high hole concentration.

4. Conclusions

In summary, we have demonstrated significant tuning of IX energy in $Mo_xW_{1-x}Se_2/WSe_2$ and $Mo_xW_{1-x}Se_2/MoSe_2$ alloy heterostructures by changing the Mo composition *x*. We use PL measurements at 10 K, where we observe a shift of IX PL energy by 130 meV in $Mo_xW_{1-x}Se_2/WSe_2$ as a function of *x*, as well as an unusual asymptotic dependence of IX PL energy approaching the homobilayer configuration. We show that this behavior stems from strong hybridization between conduction states of the WSe_2 and alloyed layers for $x < 0.65$, when the interlayer conduction band offset falls below ≈250 meV, leading to a $K - Q$ indirect bandgap for the heterostructure, and thus changing the nature of the IX. We probed the effects of such strong bandstructure modifications on IX also by means of time-resolved PL experiments and by measuring PL power dependences, supporting our conclusion about the transition to an indirect bandgap in the HBLs with $x < 0.65$. We also find similar effects in $Mo_xW_{1-x}Se_2/MoSe_2$ HBLs. As background information, we also extract detailed energy dependences of A- and B- excitons, A* trions and IX in monolayer and bilayer $Mo_xW_{1-x}Se_2$ as a function of *x*.

This work demonstrates the potential of adopting TMD alloys in vdW heterobilayers to achieve continuous bandstructure tuning, and fine band hybridization engineering. Tuning the A-exciton energy and band-edge offsets using alloying provides an additional probing approach for lattice reconstruction phenomena, currently actively being discussed in theory and observed in microscopy and optical spectroscopy experiments.[27–30]

5. Experimental Section

Fabrication of alloy HSs: High-quality fully encapsulated HBL samples were fabricated using PMMA-assisted dry-peel transfer. To minimize contamination, heterostructures were fabricated using a remotely controlled micromanipulation setup placed inside an argon chamber with <0.1 ppm O_2 and H_2O. The bulk crystals were mechanically exfoliated onto a 90 nm layer of PMMA coated on a silicon wafer. Monolayers were then identified via optical microscopy, as well as through luminescence imaging in the

dark-field configuration. Crystals that had adjacent straight edges at 0°, 60°, or 120° to one another (indicating one of the crystallographic axes) were then selected and picked up onto an hBN film (less than around 10 nm thickness) held by a PMMA membrane. During the transfer of the second TMD layer the edges were aligned to within 0.5° of the desired angle and finally transferred onto another hBN film (less or around 20 nm thickness) exfoliated onto an oxidized silicon wafer (70 nm SiO_2) to achieve full encapsulation. To prevent spontaneous rotation of the TMD layers and deterioration of $MoSe_2$ crystalline quality, exposure of the heterostructures to temperatures greater than 70°C was avoided. See further details of the fabrication procedure in Note S1 (Supporting Information).

Optical Measurements: The photoluminescence images of the heterobilayer samples were acquired using a modified bright-field microscope (LV150N, Nikon) equipped with a colour camera (DS-Vi1, Nikon). The near-infrared emission from the white-light source was blocked with a 550-nm short-pass filter (FESH0550, Thorlabs), and a 600-nm long-pass filter (FELH0600, Thorlabs) was used to isolate the photoluminescence signal from the sample.

Spectrally-resolved photoluminescence and reflectance contrast measurements were performed using a custom-built microphotoluminescence setup. For photoluminescence, the excitation light centred at 2.33 eV was generated by a diode-pumped solid-state laser (CW532-050, Roithner), whereas for reflectance contrast a stabilized tungsten-halogen white-light source (SLS201L, Thorlabs) was used. The excitation light was focused onto the sample using a 50x objective lens (M Plan Apo 50X, Mitutoyo). The photoluminescence and reflectance contrast signals collected in the backwards direction were detected by a 0.5-m spectrometer (HRS-500, Princeton Instruments) with a nitrogen-cooled charge-coupled device camera (PyLoN:100BR, Princeton Instruments). The photoluminescence signal was isolated using a 550-nm short-pass filter (FELH0550, Thorlabs). The reflectance contrast spectra were derived by comparing the spectra of white light reflected from the sample and the substrate as $RC(\lambda) = (R(\lambda) - R0(\lambda))/(R0(\lambda))$, where R (R0) is the intensity of light reflected by the sample (substrate). The room-temperature measurements were performed in ambient conditions. The low-temperature measurements were carried out using a continuous-flow liquid helium cryostat, in which the sample was placed on a cold finger with a base temperature of 10 K.

To acquire the PL decay of the IX in the entire set of samples, the emitted photons were detected with an avalanche diode photodetector (APD) (ID100-MMF50), with a timing resolution of ~40 ps, and a photon counting card (SPC-130). A 638 nm pulsed diode laser (PicoQuant LDH) was used as excitation source, with 80 MHz repetition rate, which resulted in a instrument response function (IRF) with ≈150 ps FWHM.

Supporting Information

Supporting Information is available from the Wiley Online Library or from the author.

Acknowledgements

A.C., L.S.., R.P., K.E., and A.I.T. acknowledge financial support of the European Commission H2020-MSCA-ITN project under grant agreements 676108. A.G., C.L., D.J.G., E.A., and A.T. acknowledge financial support of the European Graphene Flagship Projects under grant agreements 785219 and 881603 and EPSRC grants EP/V006975/1, EP/V026496/1, EP/V034804/1, and EP/S030751/1. V.F. and K.E. acknowledge financial support of the European Graphene Flagship Project under grant agreement 881603. A.G. acknowledges support by the European Union project ENOSIS H2020-MSCA-IF-2020-101029644. K.W. and T.T. acknowledge support from the JSPS KAKENHI (Grant Numbers 20H00354, 21H05233, and 23H02052) and World Premier International Research Centre Initiative (WPI), MEXT, Japan. D.A.R.T. acknowledges funding from PAPIIT-DGAPA-UNAM grant IA106523. L.S. acknowledges support through a Humboldt Research Fellowship from the Alexander von Humboldt Foundation. K.S.N. acknowledges support from the Ministry of Education, Singapore (Research Centre of Excellence award to the Institution for Functional Intelligent Materials, I-FIM, project No EDUNC-33-18-279-V12) and from the Royal Society (UK, grant number RSRP\R\190000). V.F. acknowledges EPSRC grants EP/V007033/1 and EP/S030719/1.

Conflict of Interest

The authors declare no conflict of interest.

Author Contributions

A.C., R.P., L.H., A.K., and C.L. fabricated heterostructure samples. K.W. and T.T. synthesized the high quality hBN. A.C., A.G., C.L., D.J.G., L.S., and E.A. carried out optical spectroscopy measurements. A.C., A.G., and C.L. analyzed the data with contribution from D.J.G., L.S., E.A., A.I.T. and D.A.R.T. D.A.R.T. and V.F. developed theory. A.G., C.L., A.I.T., and D.A.R.T. wrote the manuscript with contribution from all co-authors. A.I.T., K.E., and K.S.N. managed various experimental aspects of the project. A.I.T. conceived and supervised the project.

Data Availability Statement

The data that support the findings of this study are available from the corresponding author upon reasonable request.

Keywords

2D materials, heterobilayers, interlayer excitons, semiconductors, transition metal dichalcogenides, van der Waals heterostructures

Received: September 18, 2023
Revised: December 20, 2023
Published online:

[1] A. K. Geim, I. V. Grigorieva, *Nature* **2013**, *499*, 419.
[2] K. Novoselov, A. Mishchenko, A. Carvalho, A. C. Neto, *Science* **2016**, *353*, aac9439.
[3] Y. Tang, J. Gu, S. Liu, K. Watanabe, T. Taniguchi, J. Hone, K. F. Mak, J. Shan, *Nat. Nanotechnol.* **2021**, *16*, 52.
[4] J. Kang, S. Tongay, J. Zhou, J. Li, J. Wu, *Appl. Phys. Lett.* **2013**, *102*, 22.
[5] C. Gong, H. Zhang, W. Wang, L. Colombo, R. M. Wallace, K. Cho, *Appl. Phys. Lett.* **2013**, *103*, 1.
[6] D. Huang, J. Choi, C.-K. Shih, X. Li, *Nat. Nanotechnol.* **2022**, *17*, 227.
[7] D. Schmitt, J. P. Bange, W. Bennecke, A. AlMutairi, G. Meneghini, K. Watanabe, T. Taniguchi, D. Steil, D. R. Luke, R. T. Weitz, S. Steil, G. S. Matthijs Jansen, S. Brem, E. Malic, S. Hofmann, M. Reutzel, S. Mathias, *Nature* **2022**, *608*, 499.
[8] T. Li, S. Jiang, L. Li, Y. Zhang, K. Kang, J. Zhu, K. Watanabe, T. Taniguchi, D. Chowdhury, L. Fu, J. Shan, K. F. Mak, *Nature* **2021**, *597*, 350.
[9] E. M. Alexeev, D. A. Ruiz-Tijerina, M. Danovich, M. J. Hamer, D. J. Terry, P. K. Nayak, S. Ahn, S. Pak, J. Lee, J. I. Sohn, M. R. Molas, M. Koperski, K. Watanabe, T. Taniguchi, K. S. Novoselov, R. V. Gorbachev, H. S. Shin, V. I. Fal'ko, A. I. Tartakovskii, *Nature* **2019**, *567*, 81.
[10] N. P. Wilson, W. Yao, J. Shan, X. Xu, *Nature* **2021**, *599*, 383.
[11] K. Tran, G. Moody, F. Wu, X. Lu, J. Choi, K. Kim, A. Rai, D. A. Sanchez, J. Quan, A. Singh, J. Embley, A. Zepeda, M. Campbell, T. Autry, T. Taniguchi, K. Watanabe, N. Lu, S. K. Banerjee, K. L. Silverman, S. Kim, E. Tutuc, L. Yang, A. H. MacDonald, X. Li, *Nature* **2019**, *567*, 1.

[12] A. J. Jones, R. Muzzio, S. Pakdel, D. Biswas, D. Curcio, N. Lanatà, P. Hofmann, K. M. McCreary, B. T. Jonker, K. Watanabe, T. Taniguchi, S. Singh, R. J. Koch, C. Jozwiak, E. Rotenberg, A. Bostwick, J. A. Miwa, J. Katoch, S. Ulstrup, *2D Mater.* **2021**, *9*, 015032.
[13] N. R. Wilson, P. V. Nguyen, K. Seyler, P. Rivera, A. J. Marsden, Z. P. L. Laker, G. C. Constantinescu, V. Kandyba, A. Barinov, N. D. M. Hine, X. Xu, D. H. Cobden, *Sci. Adv.* **2017**, *3*, 1.
[14] H. Baek, M. Brotons-Gisbert, Z. X. Koong, A. Campbell, M. Rambach, K. Watanabe, T. Taniguchi, B. D. Gerardot, *arXiv preprint arXiv:2001.04305* **2020**.
[15] Y. Tang, L. Li, T. Li, Y. Xu, S. Liu, K. Barmak, K. Watanabe, T. Taniguchi, A. H. MacDonald, J. Shan, K. F. Mak, *Nature* **2020**, *579*, 353.
[16] Y. Xu, K. Kang, K. Watanabe, T. Taniguchi, K. F. Mak, J. Shan, *Nat. Nanotechnol.* **2022**, *17*, 934.
[17] Y. Shimazaki, I. Schwartz, K. Watanabe, T. Taniguchi, M. Kroner, A. Imamoğlu, *Nature* **2020**, *580*, 472.
[18] P. Rivera, J. R. Schaibley, A. M. Jones, J. S. Ross, S. Wu, G. Aivazian, P. Klement, K. Seyler, G. Clark, N. J. Ghimire, J. Yan, D. G. Mandrus, W. Yao, X. Xu, *Nat. Commun.* **2015**, *6*, 1.
[19] P. Rivera, H. Yu, K. L. Seyler, N. P. Wilson, W. Yao, X. Xu, *Nat. Nanotechnol.* **2018**, *13*, 1.
[20] Y. Jiang, S. Chen, W. Zheng, B. Zheng, A. Pan, *Light: Sci. Appl.* **2021**, *10*, 72.
[21] S. Adachi, *Properties of semiconductor alloys: group-IV, III-V and II-VI semiconductors*, vol. 28, John Wiley & Sons, **2009**.
[22] L. Xie, *Nanoscale* **2015**, *7*, 18392.
[23] G. Wang, C. Robert, A. Suslu, B. Chen, S. Yang, S. Alamdari, I. C. G., T. Amand, X. Marie, S. Tongay, B. Urbaszek, *Nat. Commun.* **2015**, *6*, 1.
[24] J. Ye, B. Niu, Y. Li, T. Li, X. Zhang, *Appl. Phys. Lett.* **2017**, *111*, 152106.
[25] L. Li, W. Zheng, C. Ma, H. Zhao, F. Jiang, Y. Ouyang, B. Zheng, X. Fu, P. Fan, M. Zheng, Y. Li, Y. Xiao, W. Cao, Y. Jiang, X. Zhu, X. Zhuang, A. Pan, *Nano Lett.* **2020**, *20*, 3361.
[26] Y. Zi, C. Li, C. Niu, F. Wang, J.-H. Cho, Y. Jia, *J. Phys.: Condens.Matter* **2019**, *31*, 435503.
[27] A. Weston, Y. Zou, V. Enaldiev, A. Summerfield, N. Clark, V. Zólyomi, A. Graham, C. Yelgel, S. Magorrian, M. Zhou, J. Zultak, D. Hopkinson, A. Barinov, T. H. Bointon, A. Kretinin, N. R. Wilson, P. H. Beton, V. I. Fal'ko, S. J. Haigh, R. Gorbachev, *Nat. Nanotechnol.* **2020**, *15*, 592.
[28] V. V. Enaldiev, V. Zólyomi, C. Yelgel, S. J. Magorrian, V. I. Fal'ko, *Phys. Rev. Lett.* **2020**, *124*, 206101.
[29] S. Magorrian, V. Enaldiev, V. Zólyomi, F. Ferreira, V. I. Fal'ko, D. A. Ruiz-Tijerina, *Phys. Rev. B* **2021**, *104*, 125440.
[30] S. Zhao, Z. Li, X. Huang, A. Rupp, J. Göser, I. A. Vovk, S. Y. Kruchinin, K. Watanabe, T. Taniguchi, I. Bilgin, A. S. Baimuratov, A. Högele, *Nat. Nanotechnol.* **2023**, *18*, 572.
[31] E. M. Alexeev, A. Catanzaro, O. V. Skrypka, P. K. Nayak, S. Ahn, S. Pak, J. Lee, J. I. Sohn, K. S. Novoselov, H. S. Shin, A. I. Tartakovskii, *Nano Lett.* **2017**, *17*, 5342.
[32] X. Hong, J. Kim, S.-F. Shi, Y. Zhang, C. Jin, Y. Sun, S. Tongay, J. Wu, Y. Zhang, F. Wang, *Nat. Nanotechnol.* **2014**, *9*, 1.
[33] P. Rivera, J. R. Schaibley, A. M. Jones, J. S. Ross, S. Wu, G. Aivazian, P. Klement, K. Seyler, G. Clark, N. J. Ghimire, J. Yan, D. G. Mandrus, W. Yao, X. Xu, *Nat. Commun.* **2015**, *6*.
[34] J. Kopaczek, T. Wozniak, M. Tamulewicz-Szwajkowska, S. J. Zelewski, J. Serafinczuk, P. Scharoch, R. Kudrawiec, *ACS omega* **2021**, *6*, 19893.
[35] A. R. Denton, N. W. Ashcroft, *Phys. Rev. A* **1991**, *43*, 3161.
[36] S. Tongay, D. S. Narang, J. Kang, W. Fan, C. Ko, A. V. Luce, K. X. Wang, J. Suh, K. D. Patel, V. M. Pathak, J. Li, J. Wu, *Appl. Phys. Lett.* **2014**, *104*, 1.
[37] M. Zhang, J. Wu, Y. Zhu, D. O. Dumcenco, J. Hong, N. Mao, S. Deng, Y. Chen, Y. Yang, C. Jin, S. H. Chaki, Y.-S. Huang, J. Zhang, L. Xie, *ACS Nano* **2014**, *8*, 7130.
[38] M. R. Molas, K. Nogajewski, A. O. Slobodeniuk, J. Binder, M. Bartos, M. Potemski, *Nanoscale* **2017**, *9*, 13128.
[39] B. Miller, A. Steinhoff, B. Pano, J. Klein, F. Jahnke, A. Holleitner, U. Wurstbauer, *Nano Lett.* **2017**, *17*, 5229.
[40] E. Barré, O. Karni, E. Liu, A. L. O'Beirne, X. Chen, H. B. Ribeiro, L. Yu, B. Kim, K. Watanabe, T. Taniguchi, K. Barmak, C. H. Lui, S. Refaely-Abramson, F. H. Da Jornada, T. F. Heinz, *Science* **2022**, *376*, 406.
[41] J. Lindlau, M. Selig, A. Neumann, L. Colombier, J. Förste, V. Funk, M. Förg, J. Kim, G. Berghäuser, T. Taniguchi, K. Watanabe, F. Wang, E. Malic, A. Högele, *Nat. Commun.* **2018**, *9*, 1.
[42] J. Holler, M. Selig, M. Kempf, J. Zipfel, P. Nagler, M. Katzer, F. Katsch, M. V. Ballottin, A. A. Mitioglu, A. Chernikov, P. C. M. Christianen, C. Schüller, A. Knorr, T. Korn, *Phys. Rev. B* **2022**, *105*, 085303.
[43] S. Ovesen, S. Brem, C. Linderälv, M. Kuisma, T. Korn, P. Erhart, M. Selig, E. Malic, *Commun. Phys.* **2019**, *2*, 23.
[44] G. Wang, X. Marie, L. Bouet, M. Vidal, A. Balocchi, T. Amand, D. Lagarde, B. Urbaszek, *Appl. Phys. Lett.* **2014**, *105*, 1.
[45] Z. Wang, Y.-H. Chiu, K. Honz, K. F. Mak, J. Shan, *Nano Lett.* **2018**, *18*, 137.
[46] G. Wang, X. Marie, L. Bouet, M. Vidal, A. Balocchi, T. Amand, D. Lagarde, B. Urbaszek, *Appl. Phys. Lett.* **2014**, *105*, 182105.
[47] D. Sun, Y. Rao, G. A. Reider, G. Chen, Y. You, L. Bre?zin, A. R. Harutyunyan, T. F. Heinz, *Nano Lett.* **2014**, *14*, 5625.
[48] V. Kravtsov, A. D. Liubomirov, R. V. Cherbunin, A. Catanzaro, A. Genco, D. Gillard, E. M. Alexeev, T. Ivanova, E. Khestanova, I. A. Shelykh, A. I. Tartakovskii, M. S. Skolnick, D. N. Krizhanovskii1, I. V. Iorsh, *2D Mater.* **2021**, *8*, 025011.